# INFLUENCE OF THE BOUNDARY LAYER STATE ON THE TRANSITION OF A DUAL-BELL NOZZLE

1. A. Barklage[1], R. Radespiel[1],
[1]Institute of Fluid Mechanics, TU Braunschweig, Braunschweig, D-38108, Germany

**Abstract**

The wake flow jet interaction of a generic space launcher with an integrated dual-bell nozzle as main propulsion unit is investigated with special regard to the boundary layer state inside the nozzle. Results were obtained by experimental measurements in a supersonic wind tunnel facility and by numerical RANS simulations. A dual-bell nozzle is an altitude compensating nozzle that promises a significant payload gain compared to conventional nozzles. Though the dual-bell nozzle was investigated in several previous studies, the interaction with an outer flow was not analysed yet. First studies with a supersonic outer flow showed an unsteady separation known as flip-flop effect in the nozzle for a wide range of nozzle total pressures. The origin of this phenomenon is not known; it could be caused by a laminar boundary layer in the nozzle. Therefore, experimental measurements with boundary layer tripping in the form zig-zag tape applied in the nozzle are conducted. Numerical RANS simulations with transition prescription are used to verify an appropriate position for the zig-zag tape. It turns out, that the zig-zag tape has a significant influence on the transition between the different operating modes of the nozzle, which is shifted to lower chamber pressures. However, the appearance of the flip-flop effect was not avoided by the use of boundary layer tripping.

## NOMENCLATURE

**Abbreviations**

| | |
|---|---|
| Re | Reynolds number, - |
| Sr | Strouhal number, - |
| M | Mach number, - |
| $\delta$ | tripping height, µm |
| u | velocity, m/s |
| p | pressure, bar |
| D | main body diameter, mm |
| HLB | Hypersonic Ludwieg tube Braunschweig |
| NPR | nozzle pressure ratio, - |
| TSA | jet simulation facility |

**Subscripts**

| | |
|---|---|
| $\infty$ | Freestream value |
| $0$ | Total value |
| $D$ | based on main body diameter |
| $sc$ | settling chamber |
| $sep$ | Separation |
| $rms$ | Root-mean-square Value |

**Superscripts**

| | |
|---|---|
| ‘ | fluctuating part |
| + | wall unit |

## 1. INTRODUCTION

Future space transportation systems call for a reduction in operational cost since commercial launches are becoming more important in the present thus leading to an increased number of competitors in this market. The propulsion system has a strong influence on the operational costs, because the efficiency of the propulsion system directly influences on the maximum payload. The efficiency of the propulsion is essentially determined by the nozzle since the nozzle defines the expansion ratio and therefore the maximum available thrust. Until today the most convenient nozzle types are TIC (truncated ideal contour) nozzles or thrust optimized nozzles. However, with this kind of nozzle the expansion ratio is limited and is chosen so that no separation occurs inside the nozzle. Flow separation inside the nozzle should be avoided since it leads to strong side loads which can destroy the nozzle structure. Hence, the expansion ratio is limited due to a compromise between different operating modes and performance losses are induced by the non-adapted nozzle. These limitations of conventional nozzle design can be overcome by the use of altitude compensating nozzles. One possible realisation of an altitude compensating nozzle is the dual-bell nozzle [1]. The dual bell-nozzle offers a one-step altitude adaptation with two different operating modes, namely sea-level mode and altitude mode. This is realized by a contour inflection, as can be seen in FIG 1. At low altitudes the high ambient pressure leads to a fixed separation of the nozzle flow at the contour inflection, wherefore side loads are strongly reduced. With increasing altitude of the launcher and thus decreasing ambient pressure, the nozzle switches to altitude mode resulting in a higher area ratio and therefore a thrust gain is obtained.

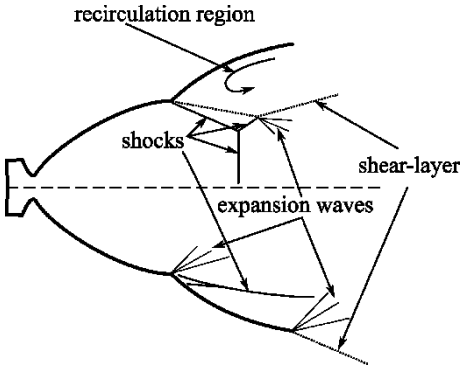


FIG 1Sketch of the operating modes of a dual-bell nozzle: sea-level mode (top) and altitude mode (bottom)

Horn and Fischer carried out first experimental measurements on dual-bell nozzles [2]. They observed additional thrust losses. During sea-level mode the pressure in the recirculation region is below the ambient pressure leading to a loss in thrust called aspiration drag. The not optimised nozzle extension leads to thrust losses in altitude mode. In addition, the transition occurs at lower pressures compared to an optimal transition, further reducing the thrust. Still, the dual-bell nozzle offers an increased thrust along the whole trajectory than conventional used nozzles, as shown by Hagemann et al. [3]. The flow phenomena for sea-level and altitude mode are now well understood and the greatest uncertainty in the design remains the transition process and the interaction with the outer flow. For this reason, many experimental [4] [5] [6] and numerical [7] [8] [9] studies were carried out on the transition process of cold-flow dual-bell nozzles. However, the interaction with the outer flow was not investigated yet.

There exists already some knowledge for the interaction of the outer flow with conventional nozzles. Investigations on a scaled Ariane V model were conducted by Reijasse and Delery [10]. They experimentally examined the flow field in the wake of a configuration containing the main engine and two boosters with a supersonic outer flow at a Mach number of 4. They performed pressure measurements, surface flow visualisations and laser doppler velocimetry and identified various three-dimensional separated zones. Schwane et al. [11] showed based on experimental measurements and numerical simulations, that unsteady loads evolve in the separated wake region for the Ariane V configuration. These loads can lead to structural vibrations on the nozzle fairing and thus can be harmful to the launcher, especially for transonic Mach numbers. A more simplified geometry consisting of two cylinders representing the main body and the nozzle fairing was investigated by Deprés and Reijasse [12] experimentally at Mach numbers of 0.6, 0.7 and 0.85 with and without jet flow. By examining unsteady wall pressure measurements, they found a peak at a Strouhal number based on the main diameter of $St_D = 0.2$, which they attributed to the shedding of large-scale vortices in the recirculation region. This configuration was investigated with zonal detached eddy simulations by Deck and Thorigny [13]. They confirmed the results found by Deprés and Reijasse and observed an additional peak at a Strouhal number of $St_D = 0.08$ corresponding to a flapping motion of the shear layer. Bitter et al. [14] performed high-repetition-rate PIV measurements on a generic launcher geometry without jet flow at Mach numbers ranging from 0.3 to 2.6. By evaluating their time-resolved results they detected no periodic vortex shedding. Janssen and Dutton [15] performed experiments in the supersonic flow regime for blunt and boattailed afterbodies. Unsteady pressure measurements at the base revealed frequency peaks at a Strouhal number of $St_D \approx 0.2$. Bannink et al. [16] and Stephan et al. [17] experimentally investigated the wake-flow of a generic launcher model with jet flow at supersonic conditions. Stephan et al. detected a distinct peak in the pressure spectra at the base at a Strouhal number of $St_D = 0.25$. Hypersonic cases were studied experimentally by Saile et al. [18] [19] and numerically by Statnikov et al. [20] [21]. Statnikov et al. performed a dynamic mode decomposition on their results and detected three dominant modes at Strouhal numbers of $St_D \approx 0.27, 0.56$ and $0.85$. They assigned the lowest frequency to a longitudinal pumping of the cavity, the medium frequency to a swinging motion of the shear layer and the highest frequency to a radial flapping motion of the shear layer.

The present study investigates the interaction of the wake flow and the jet flow on a generic launcher equipped with a dual-bell nozzle. For this purpose, experimental measurements in a short-duration facility and numerical RANS simulations are performed. Boundary layer tripping is applied inside the nozzle to determine the presence of possible laminar flow. The boundary layer state is monitored by hot film measurements. This paper is structured as follows: Initially, the geometry of the launcher model is described and the experimental and numerical setup is discussed. The results are presented based on experimental and numerical data. Finally, conclusions and an outlook are given.

## 2. EXPERIMENTAL AND NUMERICAL SETUP

### 2.1. Geometry

An overview of the geometry of the model used in this study is shown in FIG 2.This is based on a geometry that had previously been investigated in the framework of the German Collaborative Research Center Transregio 40 [17] [21]. The model consists of a cone with an apex angle of $36°$ followed by a cylinder with a diameter of $D = 108\,mm$ representing the main body. A second cylinder with an outer diameter of $d = 61\,mm$ and a length of $147.6\,mm$ is connected to the main body which represents the nozzle fairing. The inner contour of this cylinder is the dual-bell nozzle with an exit diameter of $60\,mm$. The model is supported by a sword-shaped strut that also contains the supply pipes of compressed working gas for providing the jet flow. The strut support is neglected in the numerical simulations. Approximately $100\,mm$ downstream of the models nose boundary layer tripping is applied in the experiments in order to provide a turbulent boundary-layer along the main body.

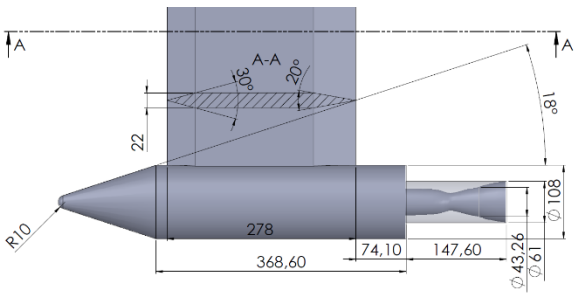


FIG 2 Geometry parameters of the investigated configuration

The base part of the nozzle is designed as a truncated ideal contour nozzle (TIC) with a design Mach number of 3.5. The nozzle contour is truncated at an axial position of approximately $40\,mm$ measured from the nozzle throat which leads to a Mach number at the exit of the base nozzle of $M = 2.54$. In order to obtain a fast transition from sea-level mode to altitude mode, the nozzle extension is designed as a constant pressure extension [3]. The nozzle extension is truncated at a length of $40.55\,mm$ so that the divergence angle at the exit is $4.7°$. The Mach number in the nozzle extension is $M = 3.024$ and transition to altitude mode is assumed to take place at a nozzle pressure ratio of $NPR = p_0/p_\infty = 12.6$. The NPR for transition was calculated based on an analytical separation criterion proposed by Génin and Stark [6].

## 2.2. Experimental setup

### 2.2.1. Wind tunnel

Experiments were carried out in the Ludwieg tube Braunschweig (HLB). The HLB is a short duration wind tunnel with a measurement time of about 80 ms. It is designed for a Mach number of 6 and consists of a 17 m long storage tube, a converging-diverging nozzle, the test section, a diffuser and a vacuum tank. A fast acting valve separates the wind tunnel into a high-pressure part and a low-pressure part. The high-pressure part consists of the storage tube and can be pressurised up to 30 bars while the first 3 meters can be heated up to 600 K. The low pressure part is evacuated to a few Millibars and flow breakdown during measurement time is avoided by the $6\,m^3$ vacuum tank. In order to obtain supersonic conditions with a Mach number of 2.9 in the test section, the original Mach 6 nozzle is replaced by a tandem nozzle consisting of a settling chamber and a Mach 2.9 Laval nozzle, as shown in FIG 3. The maximum unit Reynolds number is $Re = 17.6 \cdot 10^6\ 1/m$ which is restricted by the maximum pressure in the storage tube. A description of the wind tunnel in its original configuration can be found in [22] and the Mach 2.9 configuration is detailed in [23] and [24].

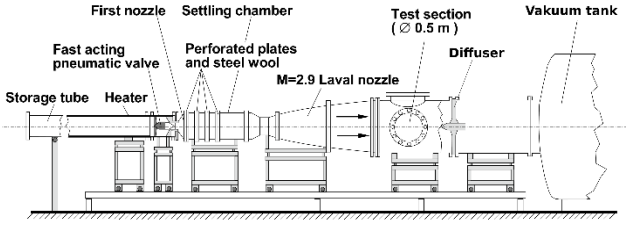


FIG 3 HLB in its supersonic configuration

### 2.2.2. Jet simulation facility

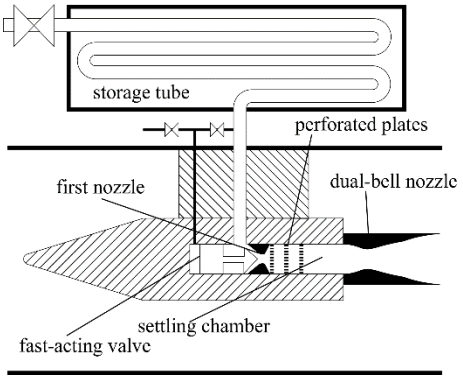


FIG 4 Sketch of the jet simulation facility

The jet simulation facility (TSA) supplies the nozzle with either pressurised air or helium and a sketch of the facility is depicted in FIG 4. The TSA uses the Ludwieg tube principle and a detailed description of the facility can be found in [17]. The 32 m long storage tube with a diameter of $18.9\,mm$ is located outside of the test section. The storage tube can be pressurised up to 140 bar and heated up to 900 K. The TSA also uses a tandem nozzle concept with a diameter of the first nozzle throat of $4\,mm$. The settling chamber has a diameter of $39\,mm$ and contains three perforated steel plates in order to improve flow quality. The settling chamber pressure is measured at the end of the settling chamber by two Keller PAA-2Mi sensors with a pressure range of 5 bar mounted in a small cavity. The total pressure in the settling chamber is calculated by one-dimensional compressible flow theory using the measured pressure and assuming a Mach number of $M_{sc} = 0.26$ in the settling chamber.

### 2.2.3. Instrumentation and test cases

The used measurement techniques in this study comprise of schlieren visualisation, unsteady pressure measurements and hot film measurements. Pressure sensors are located at the base, on the nozzle fairing and in the nozzle interior. Hot-film sensors were placed in the nozzle interior. An overview of the sensor positions is given in FIG 5.

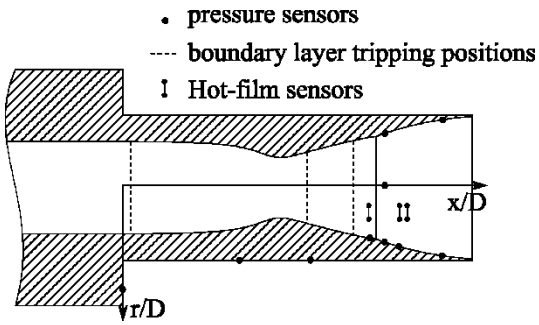


FIG 5Location of pressure sensors, hot-film sensors and boundary layer tripping

Most of the pressure sensors are located at a circumferential position of $\varphi = 180°$ measured from the strut support. A minor influence of the strut is expected at this position. The pressure was measured at four different streamwise positions of $x/D = 0.96, 1.02, 1.08$ and $1.25$ on the inner nozzle wall. The most upstream location is located in the base part of the nozzle and the remaining sensors are located in the nozzle extension. In order to measure possible unsymmetrical flow, additionally the pressure is recorded at circumferential positions of $\varphi = 90°$ and $\varphi = 0°$ at a streamwise position of $x/D = 1.02$. The pressure at the most downstream position of $x/D = 1.25$ is also measured at a circumferential position of $\varphi = 0°$. Base pressure is recorded at a radial position of $r/D = 0.42$ at three different circumferential positions of $\varphi = 180°, 190°$ and $240°$ by flush-mounting Kulite sensors, model XCQ-093. Two Kulite sensors of the type LE-062 are mounted on the nozzle fairing at a circumferential position of $\varphi = 180°$ and streamwise positions of $x/D = 0.56$ and $x/D = 1.03$, respectively. The upstream position of $x/D = 0.56$ corresponds to the estimated reattachment location.
A Spectrum M2i.4652 transient recorder sampled the pressure data at a sampling frequency of 3 MHz.

Hot-film sensors are integrated onto the inner nozzle wall to determine the boundary layer state. Three sensors are located at axial positions of $x/D = 0.96,\ 1.08$ and $1.11$. Whereas the most upstream sensor is positioned in the base part of the nozzle and the remaining sensors are positioned in the nozzle extension. Unfortunately, the two sensors at $x/D = 0.96$ and $1.08$ became faulty two times during the measurement campaign, so that reference data is only available for the sensor at $x/D = 1.11$. Therefore, only the measured data of this sensor will be discussed in the result section. A DANTEC 56C01/C17 constant temperature anemometer operated the hot-film sensors at

an overheat ratio of 0.33. The data was sampled with the same transient recorder as used for the pressure signals.

Schlieren images were taken in the wake and nozzle region for a qualitative characterisation of the flowfield. The schlieren system uses a conventional coincident setup with a continuous light source. The resulting images were recorded by a Phantom v711 camera with a minimum exposure time of $1\ \mu s$ and a maximum recording frequency of 7500 Hz at a resolution of $1280 \times 800$ px. In this study the exposure time was $5\ \mu s$ and the maximum recording frequency was 33,000 Hz at a resolution of $512 \times 384$ px.

Boundary layer tripping was applied in the nozzle at three different locations, as displayed in FIG 5 at $x/D = 0.03$, $0.72$ and $0.90$. The most upstream position is located in the subsonic part of the nozzle and the two other positions are located in the base part of the nozzle. The tripping was realized by gluing zig-zag tape of different thickness into the nozzle. The thickness of the used zig-zag tape was $\delta = 40\ \mu m, 100\ \mu m, 140\ \mu m$ and $180\ \mu m$, respectively. Experiments were carried out with and without an outer flow. In order to investigate the effectiveness of the boundary-layer tripping at different nozzle Reynolds numbers, the transition from sea-level to altitude mode was investigated at two different ambient pressures of $p_\infty = 3100\ Pa$ and $1300\ Pa$ by evacuating the test section and running the TSA alone. The investigated nozzle Reynolds number range $Re^* = \rho^*\, u^*\, d^*/\mu^* = 86{,}560 - 228{,}132$ is determined from throat conditions and the corresponding settling chamber conditions together with the wind tunnel parameters can be taken from TAB 1.

| HLB | | TSA | |
|---|---|---|---|
| $p_\infty\ [bar]$ | $4.1 \cdot 10^{-2}$ | $p_{0,SC}\ [bar]$ | $0.13 - 0.60$ |
| $T_\infty\ [K]$ | 102 | $T_0\ [bar]$ | 293 |
| $M$ | 2.9 | $Re^*$ | $86{,}560 - 228{,}132$ |
| $Re_D$ | $1.3 \cdot 10^6$ | $NPR$ | $5.6 - 19.3$ |
| $p_{0,SC}\ [bar]$ | 1.52 | | |

TAB 1 Freestream and jet simulation parameters

## 2.3. Numerical setup

### 2.3.1. Method

The DLR TAU code [25] was used to perform numerical simulations for axisymmetric flow. TAU is a finite volume solver for the compressible Navier-Stokes equations on structured and unstructured grids. In this study the solver was used to compute the steady Reynolds-Averaged-Navier-Stokes equations. Reynolds stresses are modeled by a one-equation turbulence model of Spalart and Almaras [26]. This turbulence model has shown to produce accurate results for separated nozzle flows [27] and for the prediction of transition of dual-bell nozzles [9]. Viscous terms are approximated by a second order accurate centered scheme. Euler terms are discretized using the AUSMDV upwind scheme developed by Wada and Liu [28]. An algorithm based on the Green-Gauss divergence theorem computes the gradients of the flow variables with second-order accuracy. Temporal discretisation uses a backward Euler method.
The convergence to steady state was accelerated using local time-stepping, a point explicit residual smoothing algorithm and a geometrical multigrid method.

### 2.3.2. Grid and boundary conditions

The commercial software Pointwise was used to create two-dimensional structured computational grids. The grid was adapted in order to resolve the most dominant shock waves. These include the bow shock and the internal shock in the nozzle extension. The grid which was used for all numerical calculations is shown in FIG *6* Computational grid. Every 4th grid point is shown.FIG 6. The grid has a radial extend of about 3.7 of the main body diameter. The streamwise extend of the grid is from $x/D = -5.01$ to $x/D = 3.51$, whereas the junction between main body and nozzle is located at $x/D = 0$. The grid is transformed to a suitable topology for axisymmetric calculations by a rotation of $1°$ around the x-axis. The boundary layer at the inner nozzle wall and at the shoulder of the main body is resolved as $y^+ < 1$. At the end of the nozzle fairing the $y^+$-value is below 2. The total number of cells is 211,097.

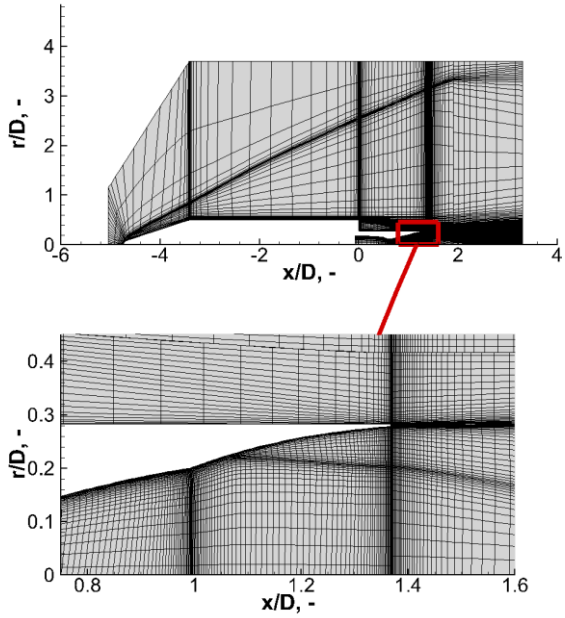


FIG 6 Computational grid. Every 4th grid point is shown.

Solid walls are represented by a no slip-condition. An isothermal condition with a temperature of $293\ K$ is applied. Axisymmetric boundaries are set in circumferential direction. The boundaries in streamwise direction are specified as supersonic inflow and supersonic outflow, respectively. At $r = 0$ a symmetry axis is specified represented by a gradient of zero in radial direction for the flow variables.

| Outer flow | | | | Nozzle flow | | |
|---|---|---|---|---|---|---|
| $M\ [-]$ | $p_\infty\ [Pa]$ | $T_\infty\ [K]$ | $Re_D\ [-]$ | Boundary layer state | $NPR$ | $T_0\ [K]$ |
| 3 | 4100 | 102 | $1.3 \cdot 10^6$ | Laminar | $3, 5, 7, 10$ | 293 |
| 3 | 4100 | 102 | $1.3 \cdot 10^6$ | Transition $x/D = 0.72$ | $3, 5, 7, 10$ | 293 |
| 3 | 4100 | 102 | $1.3 \cdot 10^6$ | Transition $x/D = 0.90$ | $3, 5, 7, 10$ | 293 |
| 3 | 4100 | 102 | $1.3 \cdot 10^6$ | turbulent | $3, 5, 7, 10$ | 293 |

TAB 2 Boundary conditions for the outer flow and the nozzle flow

A farfield condition is set at the outer radial boundary. Simulations were performed with different boundary layer states inside the nozzle, which include fully laminar flow, fully turbulent flow and flow with transition prescription. The locations for transition prescription were selected accordingly to the locations of boundary layer tripping in the experiments and can be found in TAB 2. The freestream and nozzle total conditions were kept constant for the different boundary layer states.

## 3. RESULTS

The effectiveness of the zig-zag tape on the boundary layer and the nozzle transition is determined based on experiments without an outer flow. No investigations with an outer flow were carried out for this purpose since a flip-flop behaviour was observed for these cases. The effect of boundary layer tripping on the nozzle transition with an outer flow is discussed based on the numerical simulations.

### 3.1. Flow phenomena without outer flow

Experiments were performed for two different ambient pressures corresponding to different nozzle Reynolds number ranges. The ambient pressure of $p_\infty = 3100\,Pa$ represents the value of the freestream pressure if an outer flow is present ($p_\infty = 4100\,Pa$). The lower pressure of $p_\infty = 1300\,Pa$ represents the pressure that is present at the nozzle exit under the presence of a supersonic outer flow. It was shown in a previous study [29], that transition to altitude mode is shifted to lower NPR-values for a supersonic outer flow compared to a subsonic outer flow. This is caused by an expansion of the supersonic flow at the nozzle lip, thus reducing the pressure at the nozzle exit. These two cases will be referred to as 'high Reynolds number case' and 'low Reynolds number case', respectively. For the sake of brevity, the following results will be discussed on measurements with boundary layer tripping applied at $x/D = 0.72$. Results for the remaining positions were analysed in the same manner and the outcome of these results will be highlighted. Figure 7 shows schlieren images for sea-level and altitude mode for the clean case and trip heights of $\delta = 40\,\mu m, 100\,\mu m$ and $140\,\mu m$, at the high Reynolds number condition. It is obvious, that there is a change in the shock structure if the trip height exceeds $\delta = 40\,\mu m$. The oblique shock originating at the contour inflection almost coincides at the nozzle axis for the clean case and for a trip height of $\delta = 40\,\mu m$ in seal-level mode. With increasing trip height, a pronounced normal shock emerges downstream of the nozzle exit. The same behaviour is observed for altitude mode. Not only the shock structure changes, but also the value of NPR where the nozzle switches from sea-level to altitude mode. This value is almost similar for the clean case and a trip height of $\delta = 40\,\mu m$, denoting that nozzle transition occurs at a NPR of 17.3 and 16.8, respectively. This value is much higher than the value of 12.6, as assumed in nozzle design. For trip heights of $\delta = 100\,\mu m$ and $\delta = 140\,\mu m$ there is a much better agreement with the design value and for both cases the nozzle switches to altitude mode in a NPR range of NPR=12.2-13.0. Note, that the separation criterion for calculation of the NPR for transition assumes turbulent nozzle flow and for laminar flow a higher value is expected since it is well known that laminar flow separates at lower pressure gradients than turbulent flow. This leads to the presumption that there is laminar nozzle flow in the clean case and for a trip height of $\delta = 40\,\mu m$, whereas there is turbulent nozzle flow for trip heights of $\delta = 100\,\mu m$ and $\delta = 140\,\mu m$.

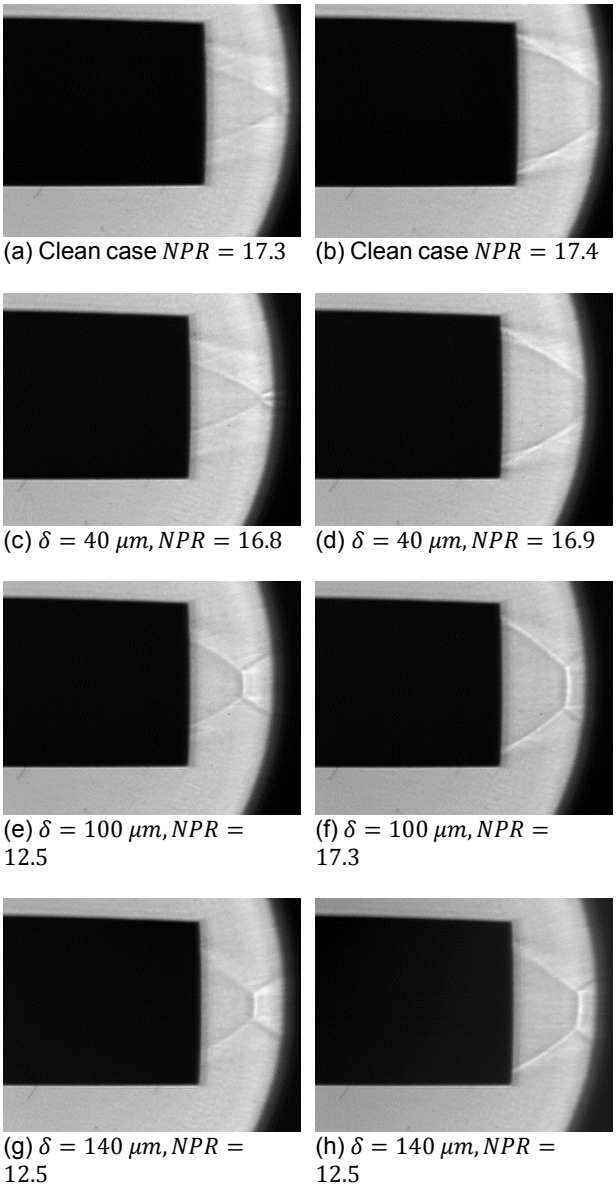

(a) Clean case $NPR = 17.3$ (b) Clean case $NPR = 17.4$

(c) $\delta = 40\,\mu m, NPR = 16.8$ (d) $\delta = 40\,\mu m, NPR = 16.9$

(e) $\delta = 100\,\mu m, NPR = 12.5$ (f) $\delta = 100\,\mu m, NPR = 17.3$

(g) $\delta = 140\,\mu m, NPR = 12.5$ (h) $\delta = 140\,\mu m, NPR = 12.5$

FIG 7 Schlieren images for sea-level (left) and altitude mode (right) for different boundary layer tripping heights $\delta$ at $x\,/\,D = 0.72$ at $p_\infty = 3100\,Pa$.

For the low Reynolds number case experiments were carried out without tripping and with zig-zag tape applied at a position of $x/D = 0.72$ with a height of $\delta = 180\,\mu m$. The higher trip height was chosen, because it was expected, that a trip height of $\delta = 100\,\mu m$ will not be effective at the low Reynolds numbers. Figure 9 shows schlieren images for three different NPR-values for the clean case and a trip height of $\delta = 180\,\mu m$ and the corresponding pressure distributions in the nozzle are displayed in FIG 8. In contrast to the previous statements at the high Reynolds number there is no noticeable change in the shock structure if

boundary layer tripping is applied.

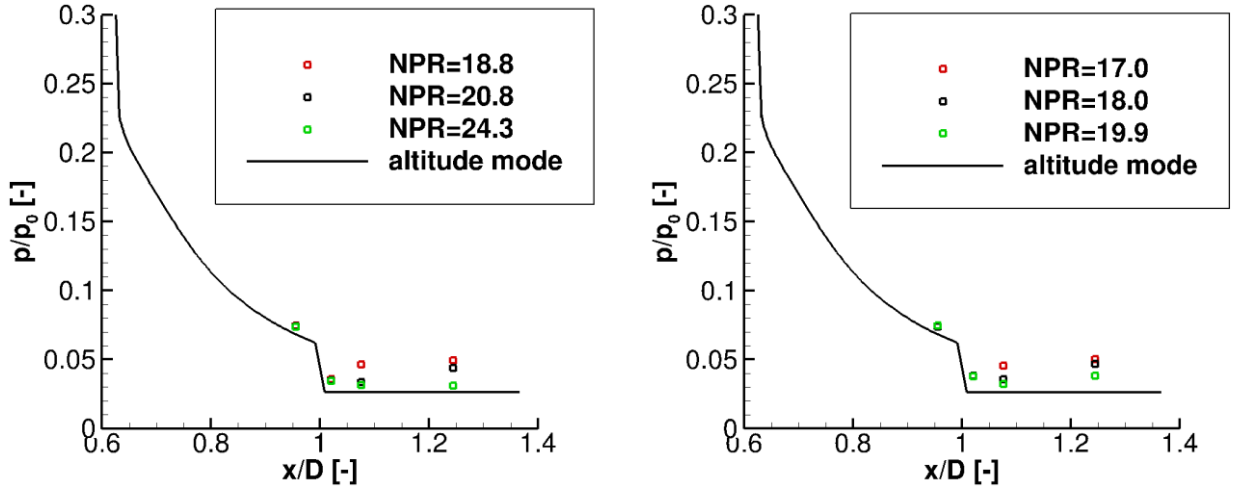


FIG 8 Mean pressure distribution inside the nozzle at different NPRs for clean case (left) and a trip height of $\delta = 180\ \mu m$ (right), at $p_\infty = 1300\ Pa$.

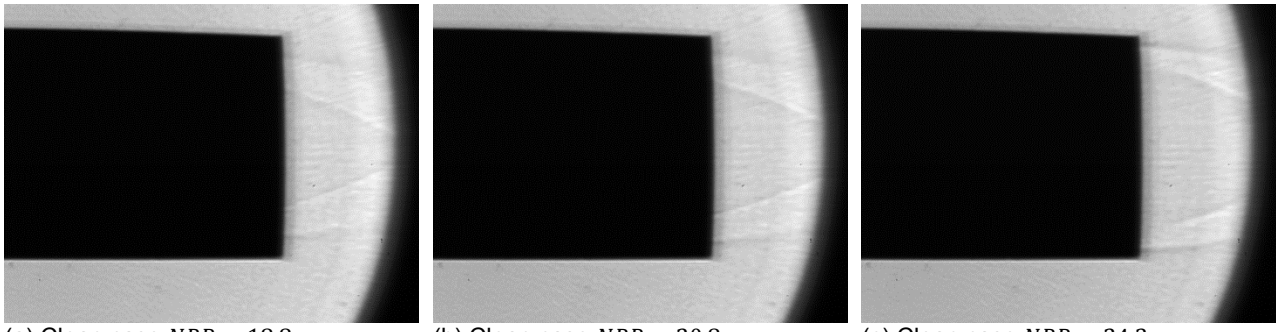

(a) Clean case $NPR = 18.8$ (b) Clean case $NPR = 20.8$ (c) Clean case $NPR = 24.3$

(d) $\delta = 180\ \mu m, NPR = 17.0$ (e) $\delta = 180\ \mu m, NPR = 18.0$ (f) $\delta = 180\ \mu m, NPR = 19.9$

FIG 9 Schlieren images for different NPRs for clean case (top) and a boundary layer tripping height of $\delta = 180\ \mu m$ (bottom) $x\ /\ D = 0.72$, at $p_\infty = 1300\ Pa$.

There is also no sudden transition from sea-level to altitude mode for the low Reynolds number case as it was observed for the high Reynolds number case. This is true for both the clean case and the case with boundary layer tripping. In the clean case the nozzle is in altitude mode at a NPR of 24.3 and in sea-level mode at a NPR of 18.8. In between the nozzle is neither in altitude or sea-level mode, which is verified by considering schlieren images and pressure distribution. This is the case for the clean case at a NPR of 20.8. The schlieren image indicates a separation of the flow in the nozzle since the origin of the shock is not located at the nozzle exit. The pressure distribution for this case demonstrates an attached flow at least to a position of $x\ /\ D = 1.08$. A separation in the nozzle can be identified by a rise in pressure above the value of altitude mode. Therefore, it can be assumed, that the nozzle flow separates between $x\ /\ D = 1.08$ and $x\ /\ D = 1.25$ since the pressure at $x\ /\ D = 1.08$ matches the altitude mode value and the pressure at $x\ /\ D = 1.25$ matches the sea-level mode value. Similar conclusions can be drawn for the case

with boundary layer tripping. There is almost no shift in the nozzle transition to lower NPR-values, if boundary layer tripping is applied. This might lead to the conclusion that a higher trip height has to be chosen to efficiently trigger boundary layer transition. This can be disproved based on laminar boundary flow theory. The boundary layer thickness is then proportional to the Reynolds number as follows: $\delta \sim \frac{1}{\sqrt{Re}}$. The factor in Reynolds number for the low Reynolds number and the high Reynolds number case is 2.4, wherefore the factor in boundary layer thickness is 1.5. Since a trip height of $\delta = 100\ \mu m$ is effective for the high Reynolds number case a trip height of $\delta = 150\ \mu m$ can be assumed to be effective at the low Reynolds number case. The ineffectiveness of boundary layer tripping for the low Reynolds number case could be caused by the tendency of the flow to relaminarise at low Reynolds numbers in conjunction with an acceleration of the flow downstream of the boundary layer tripping.

Comparable hot film data is only available for the clean case and trip heights of $\delta = 100\ \mu m$ and $\delta = 180\ \mu m$ due to difficulties in the implementation of hot film measurements on the model. The raw voltage output of the sensors was evaluated for time traces of 40 ms with constant flow conditions. Spectral quantities were computed using Welch's method based on segments consisting of 65536 points. A Hamming window was applied on the segments in order to avoid leakage effects. The quantities were averaged over 5 tunnel runs. Power spectral densities and fluctuating quantities of the hot film signals are displayed in FIG 10 at high Reynolds number condition. The spectra can be evaluated up to a maximum frequency of $Sr_D = 2$, where the amplitude of the measured signal is of the same order as the noise level. Note, that the noise spectra were evaluated based on the time signal prior to a wind tunnel run.

Only minor differences between the curves can be identified in a Strouhal number range of $Sr_D = 0.1 - 1$, where a trip height of $\delta = 180\ \mu m$ shows increased values while the curves of the clean case and a trip height of $\delta = 100\ \mu m$ almost coincide. Root mean square (RMS) values of the measured signal also show no major differences and are of the same order for the clean case and applied boundary layer tripping. Therefore, no clear statement can be made, if the boundary layer was successfully triggered to a turbulent state.

Nevertheless, the evaluation of schlieren and pressure measurements indicated a shift in the transition NPR of the nozzle to lower values caused by tripping. The effectiveness of boundary layer tripping is thus determined based on these measurements. By evaluating the two remaining tripping positions it became evident that the position at $\mathrm{x}\ /\ \mathrm{D} = 0.72$ is the most promising. The application of boundary layer tripping in the subsonic part of the nozzle at $\mathrm{x}\ /\ \mathrm{D} = 0.03$ led to no significant change in the nozzle transition or the shock pattern no matter how the height of the tripping was chosen. This result may have been caused by flow relaminarisation due to a strong acceleration in the vicinity of the nozzle throat. If boundary layer tripping is applied at $\mathrm{x}\ /\ \mathrm{D} = 0.90$ a dependency of trip height on transition NPR was observed. It is believed, that a fully turbulent boundary layer is not established when it reaches the contour inflection for tripping at $\mathrm{x}\ /\ \mathrm{D} = 0.90$.

### 3.2. Flow phenomena with outer flow

In order to determine the influence of boundary layer tripping on the nozzle transition numerical results are considered. It is clear from the previous chapter that only the tripping positions of $x\ /\ D = 0.72$ and $x\ /\ D = 0.90$ had an influence on the nozzle transition. Therefore, here these two tripping positions are compared with fully turbulent and fully laminar nozzle flow. Figure 11 left summarizes the separation position for these cases at different NPR-values that was determined by the evaluation of the friction coefficient by $c_f(x_{sep}) = 0$. There is clearly a strong change in the nozzle transition behaviour between laminar and turbulent nozzle flow as in the laminar case the nozzle switches to altitude mode at increased NPR-values.

With transition prescribed at $x\ /\ D = 0.90$ there is still a slight difference in nozzle separation to fully turbulent flow, whereas for transition prescribed at $x\ /\ D = 0.72$ the nozzle separates at almost the same position as for fully turbulent flow. This can be explained by the insufficiently short distance between the transition location of $x\ /\ D = 0.90$ and the position of the inflection point which is at $x\ /\ D = 0.99$, so that a fully turbulent boundary layer is not established. These results are in good agreement with the observations from experiments of the previous chapter, where a position of $x\ /\ D = 0.72$ showed to be the most suitable for boundary layer tripping.

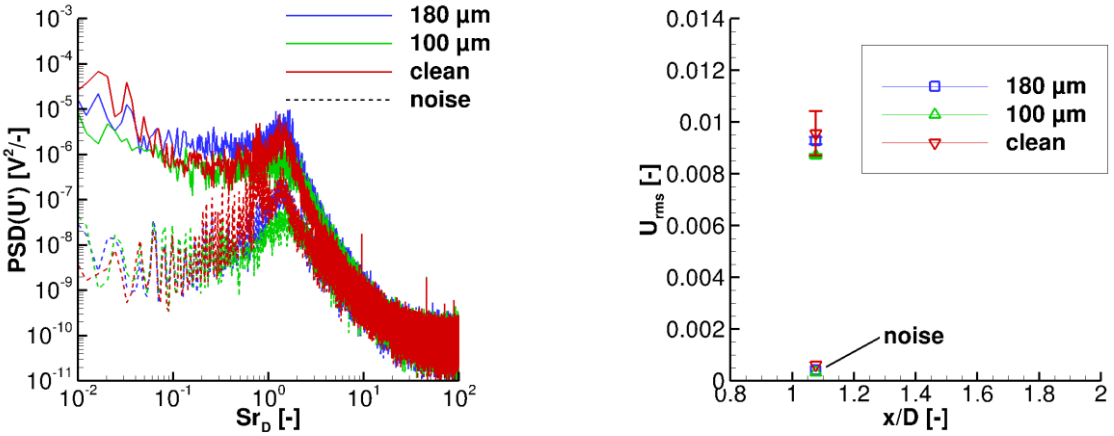


FIG 10 Power spectral densities (left) and fluctuating quantities (right) of hot film signals at high Reynolds number condition

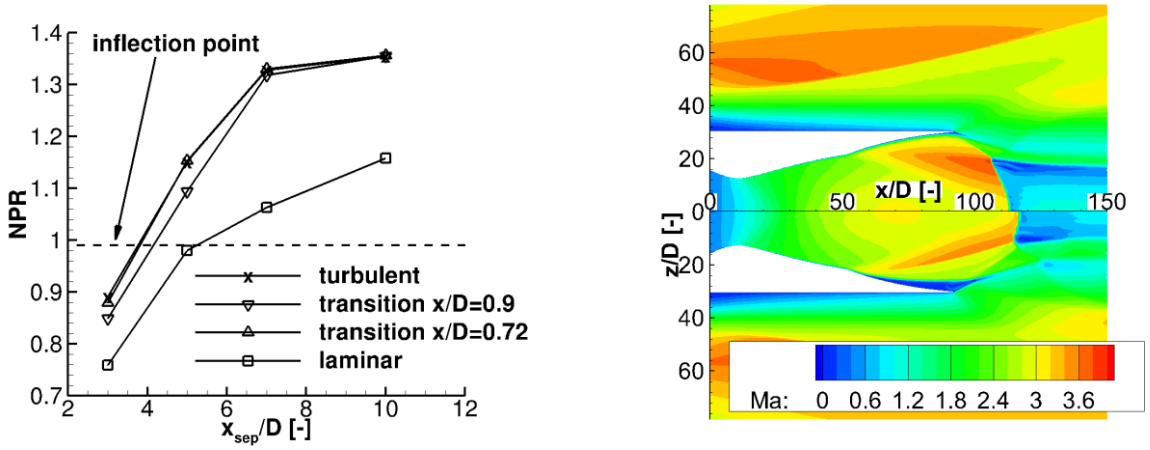


FIG 11Separation location for different boundary layer states (left) and Mach number distribution at a NPR of 7 for turbulent (top right) and laminar (bottom right) nozzle flow.

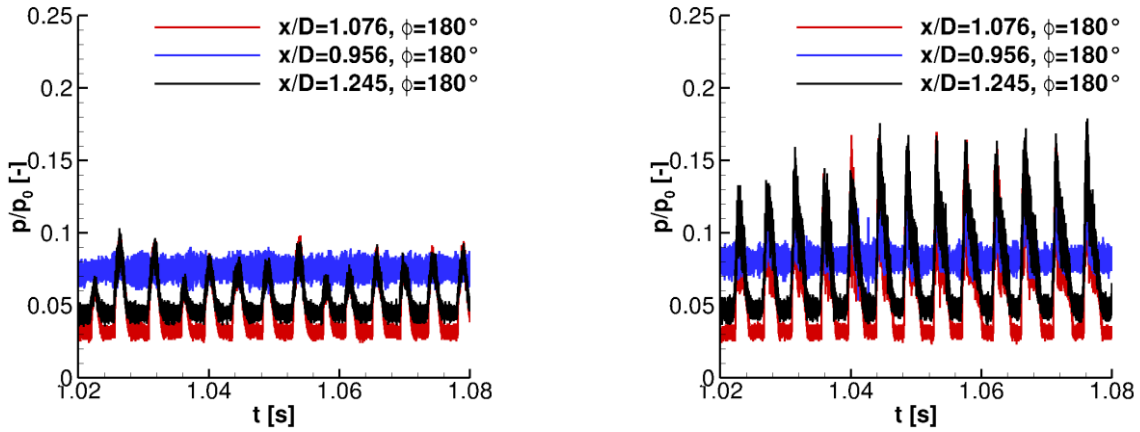


FIG 12Pressure signals at the nozzle wall at NPR=6.6 for clean case (left) and tripping applied at $x\ /\ D = 0.72$ with $\delta = 180\ \mu m$ (right)

A comparison of the flow field in terms of Mach number distribution is shown in FIG 11on the right hand side for laminar and turbulent nozzle flow at a NPR of 7. For turbulent flow the nozzle is fully flowing and an oblique shock due to the over-expansion originates at the nozzle exit while for laminar flow the oblique shock originates slightly downstream of the contour inflection. A normal shock is visible for both cases which is more strongly pronounced for the turbulent case. This is also in alignment with the experimental results, where the normal shock was also more pronounced if tripping was applied.

As mentioned earlier, a flip-flop phenomenon occurred at low settling chamber pressures in the experiments which was assumed to be associated with laminar nozzle flow. This phenomenon is clearly visible in the pressure signal of the pressure sensors located in the nozzle extension. The pressure signal for the clean case and a trip height of $\delta = 180\ \mu m$ is displayed in FIG 12. Unfortunately, the tripping did not prevent a flip-flop phenomenon of the nozzle but instead seems to support this effect since the amplitudes in the pressure signals are strongly increased compared to the clean case. However, the frequency of the flip-flop phenomenon is not changed by the tripping and is for both cases $Sr_D = 0.04$. Same observations are made for a tripping height of $\delta = 100\ \mu m$. The investigations without an outer flow revealed that boundary layer tripping is ineffective at this low Reynolds number which might explain why the flip-flop phenomenon is still occurring with tripping. A change in nozzle behaviour was also experienced without an outer flow at low Reynolds number conditions. Over a broad pressure range the nozzle was neither in sea-level or in altitude mode, but instead the nozzle flow was separating in the nozzle extension. This shows that neither sea-level or altitude mode is stable at low Reynolds numbers which might trigger the flip-flop phenomenon.

## 4. CONCLUSION

The aim of the present study was to evaluate the effect of the boundary layer state on the nozzle transition of a dual-bell nozzle. This was realised by experimental measurements in a short-duration wind tunnel and numerical RANS simulations on a generic launcher model equipped with a dual-bell nozzle. It was shown that the nozzle transition is sensitive to boundary layer tripping by applying tripping strips of different heights at three downstream positions inside the nozzle. A position of $x\ /\ D = 0.72$ located downstream of the nozzle throat in the base nozzle revealed to be the most promising position for boundary layer tripping. The NPR necessary for transition was shifted to lower values compared to the clean case by tripping and the new value was in good agreement with the design value. However, hot-film measurements could not

prove the effectiveness of the tripping. At low nozzle Reynolds numbers as present with an outer flow, boundary layer tripping became inefficient and a sudden transition to altitude mode as observed at higher Reynolds numbers did not appear.
Numerical simulations with transition prescription inside the nozzle revealed a similar behaviour as observed in experiments without outer flow. Laminar nozzle flow shifts the transition to altitude mode to higher NPR-values. A prescribed transition at $x / D = 0.72$ showed a similar separation position as fully turbulent nozzle flow, wherefore this position is considered suitable for applying boundary layer tripping. An unsteady regularly switching between sea-level and altitude mode, the so called flip-flop phenomenon, was occurring during experiments at low NPR-values. This behaviour could not be avoided by boundary layer tripping. It is believed that this behaviour is caused by low Reynolds number flow inside the nozzle. In order to increase the nozzle Reynolds number at the same NPR, the Reynolds number of the outer flow has to be increased equally. However, the wind tunnel was already operated at its highest Reynolds number and an increase can only be archived by a modification of the tandem nozzle. This is planned in the future by replacing the first nozzle throat with a higher diameter to reduce total pressure losses.

## ACKNOWLEDGEMENTS

Financial support has been provided by the German Research Foundation (Deutsche Forschungsgemeinschaft – DFG) in the framework of the Sonderforschungsbereich Transregio 40.

## REFERENCES

[1] F. B. Cowles und C. R. Foster, „Experimental study of gas-flow separation in overexpanded exhaust nozzles for rocket motors," *JPL Progress report,* pp. 4-103, 1949.

[2] M. Horn und S. Fisher, „Dual-bell altitude compensating nozzles," 1994.

[3] G. Hagemann, M. Terhardt und D. Haeseler, „Experimental and Analytical Design Verification of the Dual-Bell Concept," *Journal of Propulsion and Power,* Bd. 18, Nr. 1, pp. 116-122, 2002.

[4] S. B. Verma, R. G. C. Stark und O. Haidn, „Cold-gas experiments to study the flow separation characteristics of a dual-bell nozzle during its transition modes," *Shock Waves,* Bd. 20, pp. 191-203, 2010.

[5] C. Nürnberger-Génin und R. Stark, „Experimental Study of Dual Bell Nozzles," in *EUCASS*, 2007.

[6] C. Nürnberger-Génin und R. Stark, „Experimental study on flow transition in dual bell nozzles," *Journal of Propulsion and Power,* Bd. 26, Nr. 3, pp. 497-502, 2010.

[7] A. Wong und R. Schwane, „Numerical Investigation of Transition in Flow Separation in a Dual-Bell Nozzle," *Fourth Symposium on Aerothermodynamics for Space Vehicles,* Bd. 487, pp. 425-432, 2002.

[8] F. Nasuti, M. Onofri und E. Martelli, „Role of Wall Shape on the Transition in Axisymmetric Dual-Bell Nozzles," *Journal of Propulsion and Power,* Bd. 21, Nr. 2, pp. 243-250, 2003.

[9] D. Schneider und C. Génin, „Numerical Investigation of Flow Transition Behavior in Cold Flow Dual-Bell Rocket Nozzles," *Journal of Propulsion and Power,* Bd. 32, Nr. 5, pp. 1212-1219, 2016.

[10] P. Reijasse und J. Delery, „Investigation of the Flow past the ARIANE 5 Launcher Afterbody," *Journal of Spacecraft and Rockets,* Bd. 31, Nr. 2, pp. 208-214, 1994.

[11] R. Schwane, „Numerical Prediction and Experimental Validation of Unsteady Loads on ARIANE5 and VEGA," *Journal of Spacecraft and Rockets,* Bd. 52, Nr. 1, pp. 54-62, 2014.

[12] D. Deprés und P. Reijasse, „Analysis of Unsteadiness in Afterbody Transonic Flows," *AIAA journal,* Bd. 42, Nr. 12, pp. 2541-2550, 2004.

[13] S. Deck und P. Thorigny, „Unsteadiness of an axisymmetric separating-reattaching flow: Numerical investigation," *Physics of Fluids,* Bd. 19, pp. 1-20, 2007.

[14] M. Bitter, S. Scharnowski, R. Hain und C. J. Kähler, „High-repetition-rate PIV investigations on a generic rocket model in sub-and supersonic flows," *Experiments in fluids,* Bd. 50, Nr. 4, pp. 1019-1030, 2011.

[15] J. R. Janssen und J. C. Dutton, „Time-series analysis of supersonic base-pressure fluctuations," *AIAA journal,* Bd. 42, Nr. 3, pp. 605-613, 2004.

[16] W. Bannink, E. Houtman und P. Bakker, „Base flow/underexpanded exhaust plume interaction in a supersonic external flow," in *8th AIAA International Space Planes and Hypersonic Systems and Technologies Conference*, 1998.

[17] S. Stephan, J. Wu und R. Radespiel, „Propulsive jet influence on generic launcher base flow," *CEAS Space Journal,* Bd. 7, pp. 453-473, 2015.

[18] D. Saile und A. Guelhan, „Plume-induced effects on the near-wake region of a generic space launcher geometry," in *Proceedings of the 32nd AIAA Applied Aerodynamics Conference, AIAA*, 2014.

[19] D. Saile, A. Gülhan, A. Henckels, C. Glatzer, V. Statnikov und M. Meinke, „Investigations on the turbulent wake of a generic space launcher geometry in the hypersonic flow regime," in *Progress in Flight Physics*, 2013.

[20] V. Statnikov, S. Stephan, K. Pausch, M. Meinke, R. Radespiel und W. Schröder, „Experimental and numerical investigations of the turbulent wake flow of a generic space launcher at M= 3 and M= 6," *CEAS Space Journal,* Bd. 8, Nr. 2, pp. 101-116, 2016.

[21] V. Statnikov, T. Sayadi, M. Meinke, P. Schmid und W. Schröder, „Analysis of pressure perturbation

sources on a generic space launcher after-body in supersonic flow using zonal turbulence modeling and dynamic mode decomposition," *Physics of Fluids,* Bd. 27, Nr. 1, p. 016103, 2015.

[22] M. Estorf, T. Wolf und R. Radespiel, „Experimental and numerical investigations on the operation of the Hypersonic Ludwieg Tube Braunschweig," in *Fifth European Symposium on Aerothermodynamics for Space Vehicles*, 2005.

[23] J. Wu und R. Radespiel, „Tandem nozzle supersonic wind tunnel design," *International Journal of Engineering Systems Modelling and Simulation 47,* Bd. 5, Nr. 1-3, pp. 8-18, 2013.

[24] J. Wu und R. Radespiel, „Experimental investigation of a newly designed supersonic wind tunnel," in *Progress in Flight Physics*, 2015.

[25] D. Schwamborn, T. Gerhold und R. Heinrich, „The DLR TAU-Code: Recent Applications in Research and Industry," in *European Conference on Computational Fluid Dynamics*, Egmond aan Zee, 2006.

[26] P. R. Spalart und S. R. Allmaras, „A One-Equation Turbulence Model for Aerodynamic Flows," *La Recherche Aerospatiale: Bulletin Bimestriel de L'office National D'etudes et de Recherches Aerospatiales,* Bd. 1, pp. 5-21, 1994.

[27] R. Stark und G. Hagemann, „Current status of numerical flow prediction for separated nozzle flows," in *EUCASS*, Brussels, Belgium, 2007.

[28] Y. Wada und M.-S. Liou, „A flux splitting scheme with high-resolution and robustness for discontinuities," in *32nd Aerospace Sciences Meeting and Exhibit*, Reno, USA, 1994.

[29] A. Barklage, R. Radespiel und C. Genin, „Afterbody jet interaction of a dual-bell nozzle in supersonic flow," in *AIAA Propulsion and Energy Forum*, American Institute of Aeronautics and Astronautics, 2018, pp. --.